PAPER

Check for updates

Thermally-driven interface engineering of PMo$_{12}$/BiOBr heterojunctions for enhanced artificial photosynthesis of CO$_2$ in water vapor†

Yan Shi,[a] Shiqin Liu,[a] Hui Chen,[a] Zaihui Fu, [b] Youji Li[a] and Senpei Tang [*a]

In this study, a heterojunction material composed of Keggin-type H$_3$PMo$_{12}$O$_{40}$ and BiOBr (PM/BOB) was synthesized by a hydrothermal-calcination method, and its photocatalytic CO$_2$ reduction performance and mechanism were investigated. Structural characterization through XRD, SEM, XPS, and UV-vis DRS revealed that calcination at 200 °C facilitated tight interfacial bonding between PM and BiOBr. The BiOBr sheets fragmented into nano-sized particles that uniformly integrated with PM, while partial reduction of PM generated active species containing mixed Mo^{5+}/Mo^{6+} valence states. Under optimal conditions, the t_{200}-PM/BOB$_{0.5}$ composite demonstrated exceptional CO$_2$ reduction performance without sacrificial agents, achieving a CO production rate of 18.82 μmol g^{-1} h^{-1}, representing 10.06-fold and 7.13-fold enhancements over pristine BiOBr and PM, respectively. Mechanistic studies unveiled a Z-scheme electron transfer pathway where the reduced-state intervalence charge transfer (IVCT) excited species in PM act as electron mediators to drive CO$_2$ reduction, while the BiOBr valence band holes participate in water oxidation, achieving spatial separation of redox sites. This work provides a novel strategy for designing efficient Keggin-type molybdenum-based photocatalysts and advances the development of solar-driven CO$_2$ utilization technologies.

Introduction

The accelerated industrialization process has led to excessive consumption of fossil fuels, resulting in a sharp rise in atmospheric CO$_2$ concentration, which profoundly disrupts the global carbon balance and exacerbates the climate crisis.[1] Under this context, developing CO$_2$ utilization technologies has become a crucial pathway to achieve the "dual carbon" goals.[2] Among existing conversion strategies, photocatalytic reduction technology has attracted significant attention due to its unique advantage of directly utilizing solar energy to convert CO$_2$ into fuel molecules (CO, CH$_4$, CH$_3$OH, etc.).[3] This process triggers redox reactions through photogenerated electron–hole pairs, theoretically enabling a fully cyclic carbon-neutral process.[4] However, the inherent chemical inertness of CO$_2$ molecules (C=O bond dissociation energy reaching 750 kJ mol^{-1}) and multiple kinetic bottlenecks in photocatalytic systems (including insufficient light absorption, charge separation, and

surface reaction synergy) severely restrict practical applications.[5]

To overcome these limitations, researchers have focused on developing efficient photocatalytic systems, with the core strategy being the optimization of charge carrier dynamics and reaction microenvironments. Heterojunction engineering has emerged as an effective approach to enhance photocatalytic performance by modulating band structures to promote interfacial charge separation.[6] Most of the traditional heterostructures have been semiconductor–semiconductor composites (e.g. BiOBr/TiO$_2$, g-C$_3$N$_4$/CdS), while polyoxometalate (POM)-based heterostructures remain relatively underexplored.[7] POMs are nanoscale clusters composed of high-valence transition metals (Mo^{6+}, W^{6+}, V^{5+}, etc.) coordinated with oxygen atoms, exhibiting semiconductor-like characteristics that include:[6d,7a,8] (i) well-defined HOMO–LUMO energy gaps (2–4 eV), enabling broad-spectrum light absorption; (ii) multi-electron storage capacity (e.g., Keggin-type structures can accommodate 6–12 electrons), which is particularly suitable for the multi-step reduction of CO$_2$; and (iii) reversible redox properties that help maintain catalytic cycle stability. These unique attributes make POMs ideal building blocks for designing novel photocatalysts for CO$_2$ reduction.[8b,9]

A representative case was demonstrated by Li et al.,[10] who achieved spatially confined encapsulation of CoNi bimetallic active sites within hollow dodecahedral K$_3$PW$_{12}$O$_{40}$ frameworks through a hydrothermal-annealing synergistic strategy. This

[a] Hunan Province Key Laboratory of Mineral Cleaner Production and Green Functional Materials, College of Chemistry and Chemical Engineering, Jishou University, Jishou, 416000, Hunan, PR China. E-mail: ChemTangJSU@163.com

[b] College of Chemistry and Chemical Engineering, Hunan Normal University, 410081, Hunan, PR China

unique architecture effectively suppressed metal cluster aggregation via steric hindrance effects, yielding a CO production rate of 15.1 µmol g^{-1} h^{-1} after 6 hours of illumination in a [Ru(bpy)$_3$]$^{2+}$ photosensitizer-containing liquid-phase system. In another approach, Wang's group[9a] developed a diffusion-driven self-assembly method to precisely incorporate silicomolybdic acid into the mesoporous channels of sulfonic acid-functionalized MIL-101-Cr, constructing a hierarchical SiMo$_{12}$-O$_{40}$@SO$_3$H-MIL-101-Cr composite. This design maintained the parent material's high specific surface area and chemical stability while significantly improving active site accessibility, achieving 93.2% CO selectivity with a production rate of 82.95 µmol g^{-1} h^{-1} in triethanolamine/acetonitrile mixed solution. Such MOF pore-confined POM encapsulation strategies systematically enhance photocatalytic CO$_2$ reduction performance by creating highly dispersed atomic-level contact interfaces, enabling efficient electron transport channels and multicomponent coupling effects.[11] However, these systems represent the complex solid–liquid phase reaction mode. Although dominant in photocatalytic CO$_2$ reduction research, such three-phase systems (comprising photocatalysts, solvents, and photosensitizers/sacrificial agents) face inherent limitations:[9d,10,12] (i) poor dispersion stability of catalyst particles in liquid phase, leading to aggregation-induced deactivation; (ii) severely limited mass transfer efficiency due to low CO$_2$ solubility (e.g., ~33 mM in water) and weak adsorption capacity in conventional solvents; (iii) difficult product separation, particularly for liquid organic compounds, which substantially increases purification costs.

In contrast, the gas–solid reaction mode demonstrates distinctive advantages:[13] (i) direct utilization of CO$_2$/H$_2$O vapor as reactants not only provides proton sources but also suppresses the competitive hydrogen evolution reaction, while circumventing solvent-induced mass transfer limitations; (ii) precise control of reaction kinetics through adjustable CO$_2$ concentration; (iii) dominant gaseous products (CO, CH$_4$) enabling real-time monitoring and facile collection. Representative studies include Zhang et al. on constructing Lewis basic group-functionalized BiOBr heterojunctions through NH$_2$-UiO-66 modification. The optimized BiOBr/NH$_2$-UiO-66 exhibited a CO production rate of 9.19 µmol g^{-1} h^{-1}, representing a 4-fold enhancement over pristine BiOBr.[14] In another approach, Liu et al. developed Au@NENU-10 composite photocatalysts utilizing the dual proton-electron storage capability of Keggin-type [PTi$_2$W$_{10}$O$_{40}$]$^{7-}$ clusters, achieving 12.8 µmol per g per h CO yield under visible light irradiation.[15] Yang et al. engineered 1D/2D BiOBr/CdS heterostructures that delivered 13.6 µmol per g per h CO output through band structure optimization.[16] Nevertheless, the currently reported CO$_2$ photoreduction efficiencies in gas–solid systems remain substantially below industrial requirements. This performance gap highlights the urgent need for fundamental breakthroughs in interfacial charge transfer efficiency, CO$_2$ adsorption-activation synergy, and long-term operational stability to address existing technical bottlenecks.[13]

Notably, IVCT effects in reduced polyoxometalates provide critical advantages for CO$_2$ photoreduction.[17] As Neumann

demonstrated,[18] these mixed-valence POMs exhibit visible-light-responsive IVCT transitions ($\lambda_{max} \approx 725$ nm) through W^{5+}/W^{6+} electron hopping, enabling efficient directional electron transfer to catalytic sites. Haviv's work[19] confirmed this mechanism, showing a 3.8-fold CO yield enhancement in POM-Re hybrids via IVCT-mediated pathways. Crucially, IVCT effects simultaneously broaden light absorption to near-infrared and synchronize multi-electron transfer kinetics, effectively addressing Z-scheme recombination.

Herein, we developed a t_{200}-PM/BOB$_{0.5}$ heterojunction composite through a hydrothermal-calcination approach. Comprehensive characterization revealed that thermal treatment facilitated intimate interfacial contact between PM and BOB, while simultaneously inducing partial reduction of PM to form mixed-valence active centers (Mo^{5+}/Mo^{6+}). This structural optimization resulted in significantly enhanced visible-light absorption and charge separation efficiency. Remarkably, the t_{200}-PM/BOB$_{0.5}$ system exhibits significantly enhanced properties in CO$_2$ photoreduction performance under sacrificial agent-free and photosensitizer-free gas–solid conditions, with CO as the predominant product (selectivity ~100%). This findings provide fundamental insights for developing sustainable solar fuel generation systems with industrial viability.

Results and discussion

Microstructure and structure characterization

SEM characterization of the material reveals distinct morphological features (Fig. 1). BOB exhibits well-defined square nanosheets with smooth surfaces and uniform thickness at micro–nano scales (Fig. 1a). The PM film deposited on glass substrates displays pronounced surface undulations with extensive crack networks (Fig. 1b), which surface cracks was conducive to increasing the specific surface area and enhancing the gas adsorption capacity. The uncalcined t_{25}-PM/BOB$_{0.5}$ composite material shows that BOB and PM form a physical mixed system through mechanical grinding (Fig. 1c and d). Although a small amount of irregular fragments were generated, the main body still maintains the flake shape of BOB, indicating that the interface interaction between the components was limited when only grinding was performed. Notably, calcination at 200 °C induces significant structural reorganization in t_{200}-PM/BOB$_{0.5}$ (Fig. 1e and f), where BOB nanosheets fragment into nanoscale irregular debris while forming intimate heterointerfaces with PM, a critical microstructural foundation for multicomponent synergistic catalytic effects. EDS elemental mapping confirms homogeneous dispersion of Bi, O, Br, P, and Mo across the t_{200}-PM/BOB$_{0.5}$ surface (Fig. 1g–k).

To elucidate the surface functional groups, FT-IR spectroscopy was employed to characterize BOB, PM, and the t_{200}-PM/BOB$_{0.5}$ composite (Fig. 2a). The BOB spectrum exhibits a prominent absorption band at 514 cm^{-1}, attributed to the Bi–O stretching vibration. The PM spectrum displays four characteristic bands at 1064, 966, 867, and 719 cm^{-1}, corresponding to P–O$_a$ (oxygen atoms in PO$_4$ tetrahedra), Mo=O$_d$ (terminal oxygen atoms), Mo–O$_b$–Mo (corner-sharing bridging oxygen),
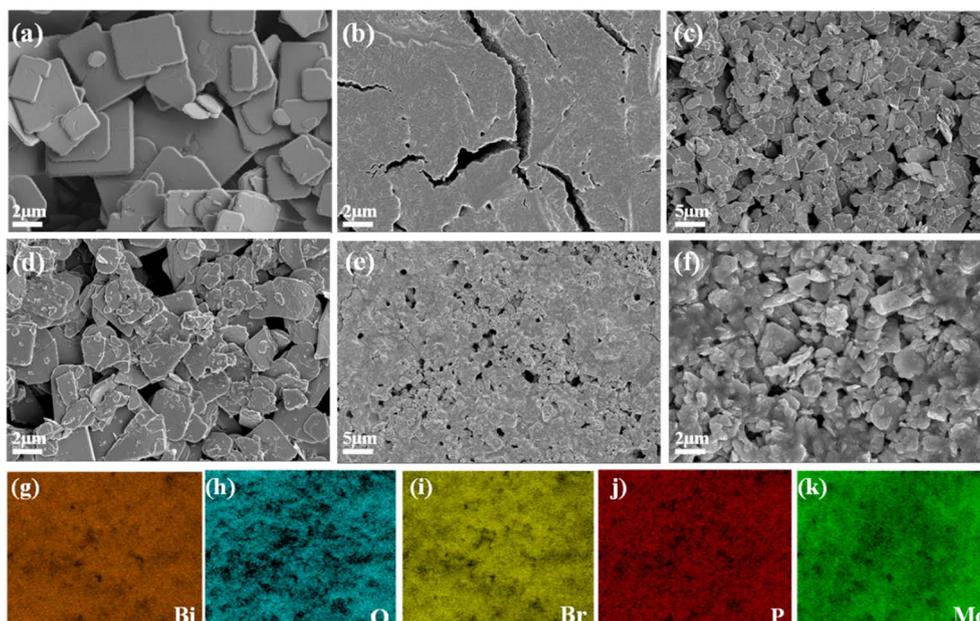
Fig. 1 SEM images of catalyst (a) BOB, (b) PM, (c and d) t_{25}-PM/BOB$_{0.5}$ and (e and f) t_{200}-PM/BOB$_{0.5}$; (g–k) elements mapping of Bi, O, Br, P, and Mo in the corresponding region.

and Mo–O$_c$–Mo (edge-sharing bridging oxygen), respectively, confirming the intact Keggin structure of PM.[20] Notably, FT-IR spectra (Fig. 2a) demonstrate that the characteristic vibration peaks of PM in the composite of t_{200}-PM/BOB$_{0.5}$ remain largely consistent with pure PM, confirming the intact preservation of its fundamental structure during compounding. The significant shift of the Bi–O vibrational characteristic peak in the t_{200}-PM/BOB$_{0.5}$ (501 cm^{-1}) compared to pure BOB, providing direct spectroscopic evidence for effective interfacial coupling between the two components.

The crystal structure of the sample was analyzed by XRD. The PM sample exhibits characteristic diffraction peaks matching the standard card (JCPDS No. 01-0032), though with reduced intensity and minor impurity peaks, indicative of its low crystallinity (Fig. S3†), which is consistent with the characteristics of this material reported in the literature.[21] In contrast, BOB and

its composites (t_{25}-PM/BOB$_{0.5}$ and t_{200}-PM/BOB$_{0.5}$) display sharp, high-intensity diffraction peaks in Fig. 2b, showing excellent agreement with the BiOBr standard card (JCPDS No. 78-0348) and confirming their high crystallinity and well-ordered atomic arrangement. The position and intensity of BOB's diffraction peak did not change significantly either by mechanical grinding or calcination at 200 °C, indicating that its crystal structure remained stable without phase change or structural damage. However, due to the material fragmentation caused by calcination process, the relative intensity of (001) crystal plane diffraction peaks decreases, while the relative intensity of (102) and (110) crystal plane diffraction peaks increases, which should be a slight change in the crystal orientation ratio due to the increase in cross section. Additionally, although PM exhibits low crystallinity and is highly dispersed within the composite, leading to weak diffraction
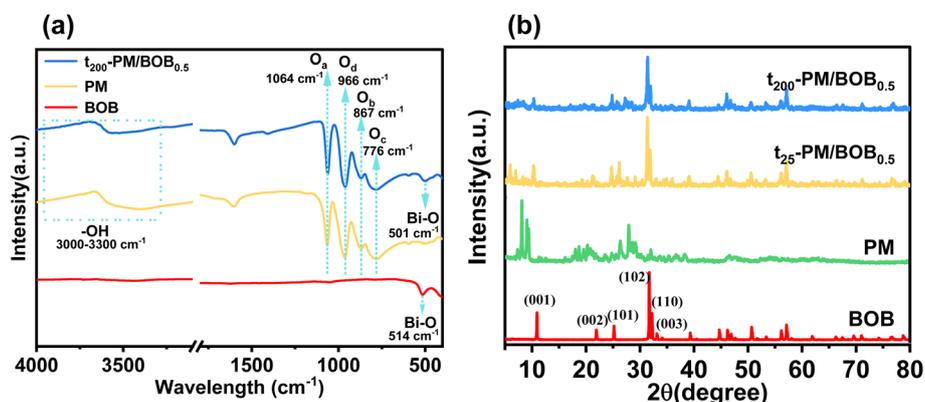

Fig. 2 (a) FT-IR spectra of BOB, PM, and t_{200}-PM/BOB$_{0.5}$; (b) the XRD pattern of BOB, t_{25}-PM/BOB$_{0.5}$, and t_{200}-PM/BOB$_{0.5}$.

signals, PM diffraction peaks could still be identified in the XRD pattern of t_{200}-PM/BOB$_{0.5}$.

The surface chemical states of the samples were characterized by XPS as shown in Fig. 4. The XPS survey spectrum (Fig. 3a) confirmed the coexistence of five elements (Bi, O, Br, P, and Mo) in the t_{200}-PM/BOB$_{0.5}$ composite, with all high-resolution spectra calibrated using the C 1s reference peak at 284.8 eV. The high-resolution Bi 4f spectrum (Fig. 3b) of pristine BOB exhibited characteristic doublet peaks at 159.6 eV (Bi $4f_{7/2}$) and 164.9 eV (Bi $4f_{5/2}$), corresponding to Bi^{3+} species.[22] Notably, the composite material showed significant positive shifts of approximately 0.4 eV in both Bi $4f_{7/2}$ (160.0 eV) and Bi $4f_{5/2}$ (165.3 eV) peaks, suggesting potential electron interaction between PM and BOB components. Similar chemical shifts were observed in the Br 3d spectrum (Fig. 3c), where the characteristic Br$^-$ peaks at 68.6 eV (Br $3d_{5/2}$) and 69.6 eV (Br $3d_{3/2}$) for BOB[23] shifted to 69.0 eV and 69.9 eV in the composite, respectively, indicating interfacial electronic redistribution. The high-resolution P 2p spectrum (Fig. 3d) revealed stable phosphorus chemical states in both PM and composite materials, showing characteristic doublet peaks at 134.2 eV (P $2p_{3/2}$) and 135.1 eV (P $2p_{1/2}$) corresponding to P^{5+} in phosphate groups.[24] For molybdenum species analysis (Fig. 3e), the PM component exhibited Mo 3d peaks at 233.4 eV (Mo $3d_{5/2}$) and 236.6 eV (Mo $3d_{3/2}$), characteristic of Mo^{6+} species.[25] In the t_{200}-PM/BOB$_{0.5}$, these peaks shift slightly to lower binding energies (233.3 eV and 236.5 eV), accompanied by additional peaks at 232.2 eV ($3d_{5/2}$) and 235.2 eV ($3d_{3/2}$) assigned to Mo^{5+}, indicating partial reduction of Mo^{6+} at the interface. The Mo^{5+} content accounts for 4.7% of total Mo species, as quantified by peak area integration.[26] In the O 1s high-resolution spectrum analysis (Fig. 3f), the peaks at 530.6 eV and 531.5 eV for BOB correspond to lattice oxygen in Bi–O bonds and surface hydroxyl groups (–OH) or adsorbed water molecules, respectively.[27] For the PM, the peaks at 531.3 eV and 532.4 eV are attributed to bridging oxygen (Mo–O–Mo) and terminal oxygen (Mo=O).[28] Because PM covers the surface of BOB, XPS detects more of the oxygen signals of the surface PM. Therefore, in the t_{200}-PM/BOB$_{0.5}$, the O 1s peaks shifted to 531.2 eV and 532.3 eV, closely aligning with PM's spectral features and exhibiting minor deviations (-0.1 eV). These XPS characterization results strongly indicate that there is an electron transfer between BOB and PM during the calcination process, which may enhance the catalytic activity by generating oxygen vacancies or exposing the active sites of Mo^{5+}.

Optical absorption and photoelectrochemical properties

The visible light absorption characteristics and the separation efficiency of photogenerated electron hole pairs of catalysts are the key factors determining their photocatalytic activity. UV-vis DRS analysis revealed distinct absorption edges for pristine BOB (450 nm) and PM (550 nm), corresponding to electron transitions in Bi–O/Bi–Br and Mo–O bonds, respectively (Fig. 4a). Remarkably, the t_{200}-PM/BOB$_{0.5}$ composite exhibited an extended absorption edge (~525 nm) with a broadened new absorption band centered at 680 nm, attributable to the IVCT effect induced by reduced Mo^{5+} species in PM. Kubelka–Munk transformation analysis yielded bandgap values of 2.79 eV (BOB), 2.28 eV (PM), and 2.34 eV (t_{200}-PM/BOB$_{0.5}$), confirming their visible-light-responsive characteristics (insert of Fig. 4a).

PL spectroscopy under 320 nm excitation provided critical verification of separation efficiency of electron–hole pairs (Fig. 4b). PM exhibited a weak emission peak at 480 nm, while BOB showed relatively intense fluorescence at 440 nm,
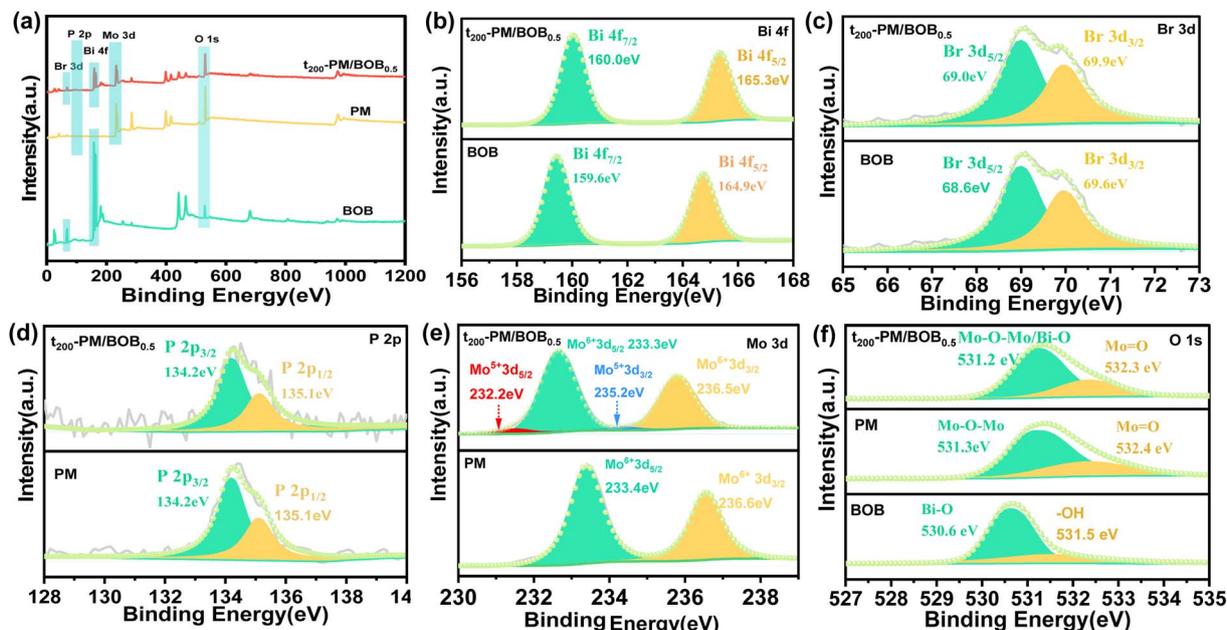

Fig. 3 (a) XPS survey spectrum and high-resolution XPS of (b) Bi 4f, (c) Br 3d, (d) P 2p, (e) Mo 3d and (f) O 1s in catalyst BOB, PM and t_{200}-PM/BOB$_{0.5}$.
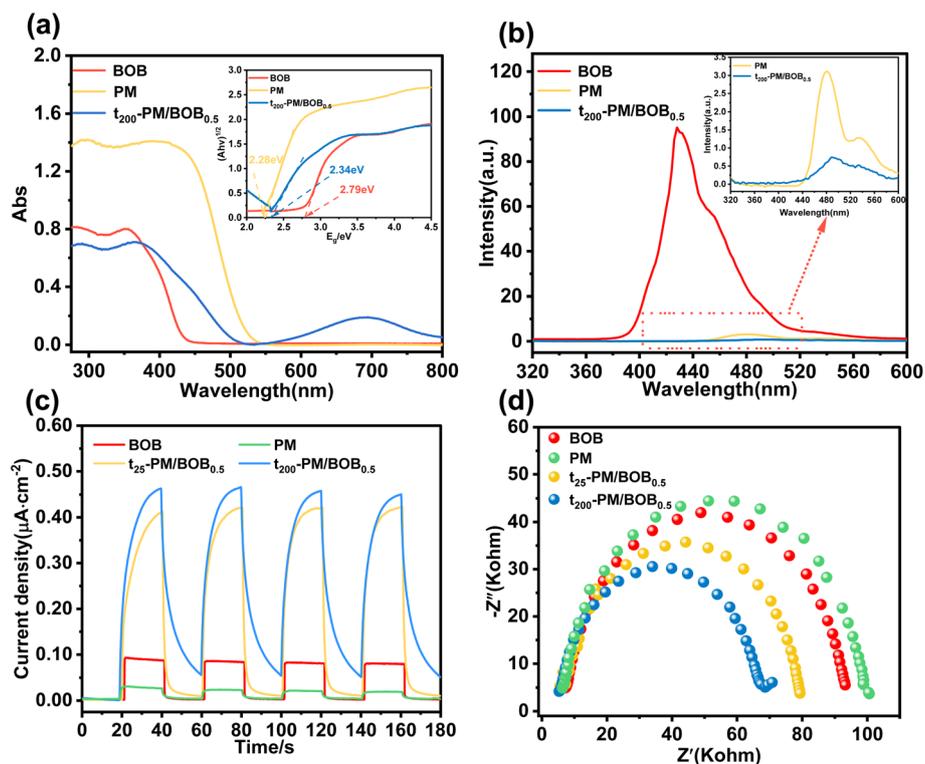
Fig. 4 (a) UV-vis DRS spectra of catalysts BOB, PM and t_{200}-PM/BOB$_{0.5}$, with the band gap diagram of the corresponding catalyst illustrated; (b) solid PL spectra of BOB, PM and t_{200}-PM/BOB$_{0.5}$, with amplified fluorescence spectra of PM and t_{200}-PM/BOB$_{0.5}$ shown in the embedded spectrogram; (c) photocurrent response and (d) EIS of BOB, PM, t_{25}-PM/BOB$_{0.5}$, and t_{200}-PM/BOB$_{0.5}$.

indicative of rapid electron–hole recombination. The t_{200}-PM/BOB$_{0.5}$ demonstrated the lowest PL intensity, verify that the interaction between BOB and PM can improve the separation efficiency of electron–hole pairs (insert of Fig. 4b). The interfacial charge transfer properties of catalysts were investigated through electrochemical characterization. As shown in Fig. 4c, the photocurrent response of t_{200}-PM/BOB$_{0.5}$ (0.46 μA cm^{-2}) significantly exceeded that of t_{25}-PM/BOB$_{0.5}$ (0.41 μA cm^{-2}), pristine BOB (0.08 μA cm^{-2}), and PM (0.03 μA cm^{-2}), indicating that the photoelectric conversion efficiency of the composite material is improved after calcination treatment. EIS analysis further revealed the charge transfer resistance through Nyquist plot comparison (Fig. 4d). The t_{200}-PM/BOB$_{0.5}$ composite exhibited the smallest arc radius, indicating the lowest interfacial charge transfer resistance among the tested materials. The quantitative correlation between the reduced semi-circular size and the improved charge separation efficiency confirms that, compared with individual components, the composite material structure significantly enhances photoinduced charge separation and interface carrier transport, which is highly consistent with the observed photocatalytic performance enhancement.

Photocatalytic CO$_2$ reduction activity

The photocatalytic CO$_2$ reduction (PCR) performance of the catalyst was investigated at gas–solid interface with water as electron sacrificial agent under simulated sunlight. As shown in Fig. 5a and b, pristine BOB and PM exhibited CO evolution rates of 1.87 and 2.64 μmol g^{-1} h^{-1}, respectively. The mechanically mixed t_{25}-PM/BOB$_{0.5}$ showed marginal improvement (3.55 μmol g^{-1} h^{-1}), whereas the calcined t_{200}-PM/BOB$_{0.5}$ achieved a remarkable 18.82 μmol g^{-1} h^{-1}, representing 10.06 and 7.13-fold enhancement over individual components. Control experiments demonstrate that individual components (uncompounded PM or BOB, denoted as t_{200}-PM and t_{200}-BOB) calcined at 200 °C for identical duration exhibited photocatalytic CO$_2$ reduction only 6.29 and 3.55 μmol g^{-1} h^{-1} respectively, showing little improvement compared with before calcination. The significant changes in catalytic performance under these different conditions highlight the key role of calcination induction interface engineering.

The calcination temperature optimization study (Fig. 5c) revealed 200 °C as the optimal thermal treatment condition. Below this threshold, insufficient heterointerface formation limited charge separation efficiency. When the temperature exceeds 200 °C, the thermal instability of PM components leads to structural decomposition, resulting in a downward trend in catalytic activity. The synchronized physical photos show that with the increase of calcination temperature (25–300 °C), the color of the material changes from light yellow to dark green (Fig. S4†), which is consistent with the characteristic color development of the reduced Mo^{5+} state of phosphomolybdenum heteropolyacid. The UV-vis DRS (Fig. S5†) further confirmed that the characteristic absorption peak intensity of
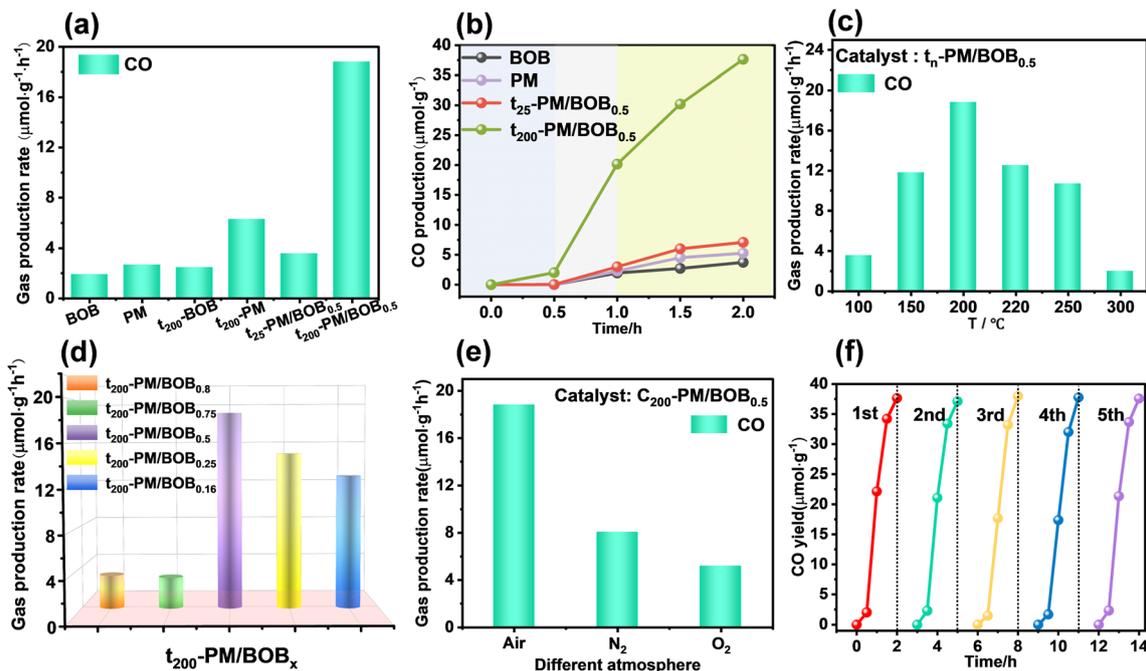
Fig. 5 (a) The PCR performance diagram of BOB, PM, t_{25}-PM/BOB$_{0.5}$, t_{200}-PM/BOB$_{0.5}$, t_{200}-BOB, t_{200}-PM and (b) their corresponding CO yields over time; (c) PCR performance diagram of t_n-PM/BOB$_{0.5}$ synthesized at different temperatures; (d) PCR performance of t_{200}-PM/BOB$_x$ with different ratios of PM/BOB; (e) The PCR performance diagram of t_{200}-PM/BOB$_{0.5}$ synthesized under different calcination atmosphere; (f) the PCR cycle test performance of t_{200}-PM/BOB$_{0.5}$.

the material at 600–800 nm was significantly enhanced with the increase of the treatment temperature, indicating that the concentration of Mo^{5+} reduced species was positively correlated with the calcination temperature.

Compositional optimization studies at 200 °C identified a 1 : 1 PM/BOB mass ratio as the optimal configuration (Fig. 5d). PM-rich composites (t_{200}-PM/BOB$_{0.8}$ and t_{200}-PM/BOB$_{0.75}$) exhibited significantly reduced activity (3.21–4.52 μmol g^{-1} h^{-1}), while BOB-dominant formulations (t_{200}-PM/BOB$_{0.25}$ and t_{200}-PM/BOB$_{0.16}$) maintained moderate performance (13.5–15.5 μmol g^{-1} h^{-1}). At the same time, different atmosphere during calcination will also affect the PCR efficiency of t_{200}-PM/BOB$_{0.5}$. As shown in Fig. 5e, when the composite material was calcined in N$_2$, air, and O$_2$ atmosphere, the CO conversion rates are 8.06, 18.82, and 5.16 μmol g^{-1} h^{-1}, respectively. This atmosphere-dependent behavior originates from dual modulation effects: (i) oxygen partial pressure regulates Mo^{5+} enrichment in PM, enhancing reducibility; (ii) calcination atmosphere tunes oxygen vacancy concentration in BOB, which serves as oxidative active sites and promotes the formation of heterojunction interface through coordination with phosphomolybdenum heteropoly acid.

The photocatalytic performance of t_{200}-PM/BOB$_{0.5}$ under varying CO$_2$ concentrations to evaluate the practical applicability of the catalyst, as illustrated in Fig. S7.† The CO production rate increased significantly from 1.33 to 18.83 μmol g^{-1} h^{-1} as the CO$_2$ concentration rose from 2 to 18 vol%. This concentration-dependent behavior demonstrates the material's direct applicability potential for medium-to-low concentration

CO$_2$ mitigation scenarios. Finally, durability tests confirmed exceptional stability of t_{200}-PM/BOB$_{0.5}$, maintaining 18.8 ± 0.24 μmol g^{-1} h^{-1}, CO production over 5 cycles with <3% activity decay (Fig. 5f). In addition, XRD and FT-IR spectra were used to conduct comparative analyses before and after the photocatalytic reaction of the t_{200}-PM/BOB$_{0.5}$. The characteristic diffraction peaks in the XRD pattern and the functional group vibrations in the FT-IR pattern all maintained their positions and intensities, and there was no obvious structural change (Fig. S6†). These robust performance stems from the engineered heterointerface's structural integrity and inherent anti-photocorrosion properties. Finally, a comparative analysis of the photocatalytic CO$_2$ reduction performance at the gas–solid interface with the recently reported POM/BiOBr-based analogues indicates that our material outperforms many of the reported similar materials, demonstrating its superior activity.

Photocatalytic mechanism

Based on the aforementioned experimental results, it can be speculated that the enhanced photocatalytic CO$_2$ reduction mechanism primarily originates from the construction of high-quality heterojunction structures. To validate this hypothesis, investigations into the band alignment and heterojunction type of the catalysts were conducted. As shown in Fig. 6a, the positive slope of the MS plot for BOB confirms its n-type semiconductor characteristics. The flat-band potential (E_{fb}) of BOB was determined to be −0.57 V. For n-type semiconductors, the E_{fb} is approximately equivalent to the Fermi level (E_F) under most
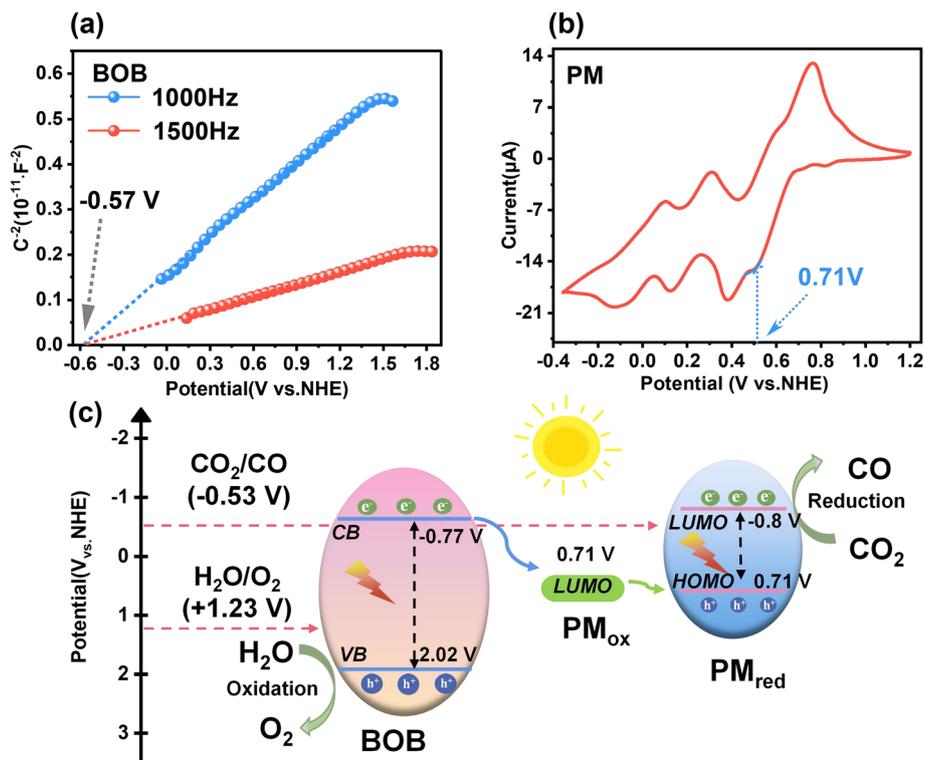
Fig. 6 (a) The M−S curve of BOB, (b) the CV curve of PM; and (c) the mechanism diagram of photocatalytic CO_2 reduction reaction based on t_{200}-PM/BOB$_{0.5}$.

conditions.[29] Based on the Boltzmann distribution relationship between E_F and conduction band potential (E_{CB}), along with the intrinsic properties of n-type semiconductors, the E_{CB} of BOB was calculated to be −0.77 V. Furthermore, the UV-vis DRS results revealed a E_g of 2.79 eV for BOB, representing the energy difference between its valence band maximum (E_{VB}) and E_{CB}. Using the equation $E_g = E_{VB} - E_{CB}$, the E_{VB} of BOB was subsequently determined as 2.02 V.

To investigate the energy band structure of PM, CV curves was employed to estimate the highest occupied molecular orbital (HOMO) and lowest unoccupied molecular orbital (LUMO) energy levels. As shown in Fig. 6b, the onset potential of the first reduction peak in the CV curve for oxidized PM (PM$_{ox}$) was measured at 0.71 V, corresponding to its LUMO potential (E_{LUMO}). Combined with the E_g of PM (2.28 eV) determined from UV-vis DRS, the HOMO potential (E_{HOMO}) was calculated as 2.79 V. Notably, the LUMO level of PM$_{ox}$ aligns with the HOMO level of reduced PM (PM$_{red}$).[30] UV-vis DRS analysis of the composite (Fig. S7†) revealed an IVCT absorption edge at 823 nm for the PM$_{red}$ component in t_{200}-PM/BOB$_{0.5}$. Using the equation $\Delta E_{gap} = 1239.8/\lambda_{edge}$, the IVCT transition bandgap was calculated as 1.51 eV. This indicates that photoexcitation induces charge transfer between Mo^{5+} and Mo^{6+} in PM$_{red}$, generating an excited state with an IVCT band (E_{IVCT}) electron reduction potential of −0.80 V.[31] Both the conduction band potential of BOB (E_{CB} = −0.77 V) and the E_{IVCT} of PM$_{red}$ are significantly more negative than the CO_2/CO reduction potential (−0.53 V *vs.* NHE),[32] confirming their thermodynamic

capability to drive CO_2 reduction to CO. Incidentally, macroscopic color changes before and after calcination of the catalyst and IVCT characteristic absorption peaks (600–900 nm) in the UV-vis DRS support the formation of reduced PM$_{red}$ (Fig. S4 and S5†), indicating partial reduction of PM in t_{200}-PM/BOB$_{0.5}$ and formation of mixed valence active centers.

Based on the aforementioned experimental results, the photocatalytic CO_2 reduction mechanism of the t_{200}-PM/BOB$_{0.5}$ composite can be summarized as follows (Fig. 6c). Under light excitation, BOB semiconductor generates photogenerated electron–hole pairs, with electrons transitioning from the valence band (VB) to the conduction band (CB). Due to the significant energy difference between the LUMO level of PM (0.71 V) and the conduction band of BOB (−0.77 V), electrons spontaneously transfer from the CB of BOB to the LUMO of PM, forming reduced PM$_{red}$ containing mixed Mo^{5+}/Mo^{6+} valence states. Studies reveal that the IVCT excited state (E_{IVCT} = −0.8 V) in PM$_{red}$ exhibits semiconductor-like impurity level characteristics, serving as an electron transfer mediator. Its reduction potential is significantly more negative than the standard CO_2/CO potential (−0.53 V), thereby efficiently driving CO_2 reduction. Simultaneously, the VB holes in BOB are consumed through water oxidation ($H_2O + h^+ \rightarrow O_2 + H^+$), achieving charge balance and supplying protons for CO_2 reduction. This Z-scheme electron transfer mechanism not only effectively suppresses carrier recombination but also significantly enhances photocatalytic efficiency through spatial separation of redox sites.

Conclusion

In general, the t_{200}-PM/BOB$_{0.5}$ composite with heterojunction structure was synthesized via hydrothermal-calcination method. Systematic characterization revealed that calcination at 200 °C facilitated intimate interfacial contact between PM and BOB, inducing partial reduction of PM to form mixed-valence active centers (Mo^{5+}/Mo^{6+}). The composite exhibited significantly enhanced visible-light absorption and charge separation efficiency. Optimization studies confirmed that air-calcination at 200 °C and a 1 : 1 PM/BOB mass ratio delivered optimal performance, achieving a CO production rate of 18.82 $\mu mol\ g^{-1}\ h^{-1}$ under gas–solid with simulated sunlight and water vapor, which was 7.1–10.6 times higher than individual components. Furthermore, the material demonstrated exceptional stability with <3% activity decay over five consecutive cycles. Mechanistic investigations attributed the superior performance to synergistic Z-scheme electron transfer and spatially separated redox sites, where the IVCT excited state in reduced PM$_{red}$ acted as an electron relay to suppress carrier recombination and accelerate CO_2 reduction kinetics. This work establishes novel design reference for developing high-performance Keggin-type molybdenum-based photocatalysts.

Data availability

The data supporting this article have been included as part of the ESI.†

Author contributions

Yan Shi: investigation, validation, formal analysis, writing – original draft. Shiqin Liu: investigation, validation. Hui Chen: investigation. Zaihui Fu: conceptualization. Youji Li: supervision. Senpei Tang: conceptualization, resources, project administration, writing – original draft, writing – review & editing.

Conflicts of interest

There are no conflicts of interest to declare.

Acknowledgements

References

1 (a) J. Martínez, F. de la Cruz-Martínez, M. A. Gaona, E. Pinilla-Peñalver, J. Fernández-Baeza, A. M. Rodríguez, J. A. Castro-Osma, A. Otero and A. Lara-Sánchez, *Inorg. Chem.*, 2019, **58**, 3396–3408; (b) W. Li, H. Wang, X. Jiang, J. Zhu, Z. Liu, X. Guo and C. Song, *RSC Adv.*, 2018, **8**, 7651–7669.

2 D. Raciti and C. Wang, *ACS Energy Lett.*, 2018, **3**, 1545–1556.

3 (a) Ž. Kovačič, B. Likozar and M. Huš, *ACS Catal.*, 2020, **10**, 14984–15007; (b) Y. Ma, X. Yi, S. Wang, T. Li, B. Tan, C. Chen, T. Majima, E. R. Waclawik, H. Zhu and J. Wang, *Nat. Commun.*, 2022, **13**, 1400; (c) S. R. Lingampalli, M. M. Ayyub and C. N. R. Rao, *ACS Omega*, 2017, **2**, 2740–2748; (d) Y.-S. Xia, M. Tang, L. Zhang, J. Liu, C. Jiang, G.-K. Gao, L.-Z. Dong, L.-G. Xie and Y.-Q. Lan, *Nat. Commun.*, 2022, **13**, 2964.

4 V. Humphrey, J. Zscheischler, P. Ciais, L. Gudmundsson, S. Sitch and S. I. Seneviratne, *Nature*, 2018, **560**, 628–631.

5 (a) B. J. Soden, W. D. Collins and D. R. Feldman, *Science*, 2018, **361**, 326–327; (b) Q. Xu, Z. Xia, J. Zhang, Z. Wei, Q. Guo, H. Jin, H. Tang, S. Li, X. Pan, Z. Su and S. Wang, *Carbon Energy*, 2023, **5**, e205.

6 (a) Y. Yu, X. Kuang, X. Jin, F. Chen, J. Min, H. Duan, J. Li, Z. Wu and B. Cao, *Appl. Surf. Sci.*, 2024, **649**, 159169; (b) M. A. Mohd Adnan, N. Muhd Julkapli, M. N. I. Amir and A. Maamor, *Int. J. Environ. Sci. Technol.*, 2019, **16**, 547–566; (c) X. Li, J. Xiong, Y. Xu, Z. Feng and J. Huang, *Chin. J. Catal.*, 2019, **40**, 424–433; (d) A. Müller, F. Peters, M. T. Pope and D. Gatteschi, *Chem. Rev.*, 1998, **98**, 239–272; (e) Y. Liu, Y. Dong, J. Yang, Y. Feng, M. Zhao, Y. Qin and H. Lv, *Chem. Commun.*, 2025, **61**, 5810–5813.

7 (a) Y. Guo and C. Hu, *J. Mol. Catal. A: Chem.*, 2007, **262**, 136–148; (b) Y.-H. Guo and C.-W. Hu, *J. Cluster Sci.*, 2003, **14**, 505–526.

8 (a) M. Stuckart and K. Y. Monakhov, *J. Mater. Chem. A*, 2018, **6**, 17849–17853; (b) K. Suzuki, N. Mizuno and K. Yamaguchi, *ACS Catal.*, 2018, **8**, 10809–10825; (c) J.-J. Ye and C.-D. Wu, *Dalton Trans.*, 2016, **45**, 10101–10112.

9 (a) Y. Wang, Y. Xie, M. Deng, T. Liu and H. Yang, *Eur. J. Inorg. Chem.*, 2021, **2021**, 681–687; (b) J. Lan, Y. Wang, B. Huang, Z. Xiao and P. Wu, *Nanoscale Adv.*, 2021, **3**, 4646–4658; (c) E. Papaconstantinou, D. Dimotikali and A. Politou, *Inorg. Chim. Acta*, 1980, **43**, 155–158; (d) J. Gu, W. Chen, G. G. Shan, G. Li, C. Sun, X. L. Wang and Z. Su, *Mater. Today Energy*, 2021, **21**, 100760; (e) J. Lan, Q. Zhu, X. Gu, M. Ma, D. Li, K. Huang, X. Fu, Y. Zhu and Y. Zhang, *Sep. Purif. Technol.*, 2023, **321**, 124228.

10 B. Li, M. Chen, Q. Hu, J. Zhu, X. Yang, Z. Li, C. Hu, Y. Li, P. Ni and Y. Ding, *Appl. Catal., B*, 2024, **346**, 123733.

11 (a) A. Solé-Daura, Y. Benseghir, M.-H. Ha-Thi, M. Fontecave, P. Mialane, A. Dolbecq and C. Mellot-Draznieks, *ACS Catal.*, 2022, **12**, 9244–9255; (b) J. Du, Y.-Y. Ma, W.-J. Cui, S.-M. Zhang, Z.-G. Han, R.-H. Li, X.-Q. Han, W. Guan, Y.-H. Wang, Y.-Q. Li, Y. Liu, F.-Y. Yu, K.-Q. Wei, H.-Q. Tan, Z.-H. Kang and Y.-G. Li, *Appl. Catal., B*, 2022, **318**, 121812; (c) H. Li, M. Chi, X. Xin, R. Wang, T. Liu, H. Lv and G.-Y. Yang, *Chin. J. Catal.*, 2023, **50**, 343–351.

12 D. Zang and H. Wang, *Polyoxometalates*, 2022, **1**, 9140006.

13 H.-N. Wang, Y.-H. Zou, H.-X. Sun, Y. Chen, S.-L. Li and Y.-Q. Lan, *Coord. Chem. Rev.*, 2021, **438**, 213906.

14 J. Liu, W. Qin, Y. Wang, Q. Xu, Y. Xie, Y. Chen, Y. Dai and W. Zhang, *Sep. Purif. Technol.*, 2024, **344**, 127289.

15 S.-M. Liu, Z. Zhang, X. Li, H. Jia, M. Ren and S. Liu, *Adv. Mater. Interfaces*, 2018, **5**, 1801062.

16 Q. Yang, W. Qin, Y. Xie, K. Zong, Y. Guo, Z. Song, G. Luo, W. Raza, A. Hussain, Y. Ling, J. Luo, W. Zhang, H. Ye and J. Zhao, *Sep. Purif. Technol.*, 2022, **298**, 121603.

17 Y. Cao, Q. Chen, C. Shen and L. He, *Molecules*, 2019, **24**, 2069.

18 H. Yu, E. Haviv and R. Neumann, *Angew. Chem., Int. Ed.*, 2020, **59**, 6219–6223.

19 E. Haviv, L. J. W. Shimon and R. Neumann, *Chem.–Eur. J.*, 2017, **23**, 92–95.

20 S. Tang, J. She, Z. Fu, S. Zhang, Z. Tang, C. Zhang, Y. Liu, D. Yin and J. Li, *Appl. Catal., B*, 2017, **214**, 89–99.

21 J. She, Z. Fu, J. Li, B. Zeng, S. Tang, W. Wu, H. Zhao, D. Yin and S. R. Kirk, *Appl. Catal., B*, 2016, **182**, 392–404.

22 T. Jia, J. Li, F. Long, F. Fu, J. Zhao, Z. Deng, X. Wang and Y. Zhang, *Crystals*, 2017, **7**, 266.

23 Y. Peng, J. Xu, T. Liu and Y.-g. Mao, *CrystEngComm*, 2017, **19**, 6473–6480.

24 (*a*) S. Damyanova, J. Fierro, I. Sobrados and J. Sanz, *Langmuir*, 1999, **15**, 469–476; (*b*) D. Barats-Damatov, L. J. Shimon, Y. Feldman, T. Bendikov and R. Neumann, *Inorg. Chem.*, 2015, **54**, 628–634.

25 L. Wang, P. Yin, J. Zhang, J. Hao, C. Lv, F. Xiao and Y. Wei, *Chem.–Eur. J.*, 2011, **17**, 4796–4801.

26 L. Wang, P. Yin, J. Zhang, J. Hao, C. Lv, F. Xiao and Y. Wei, *Chem.–Eur. J.*, 2011, **17**, 4796–4801.

27 J. Wang, J. Yang, S. Zeng, H. Liu, F. Li, H. Xie, S. Tang, Z. Fu and Y. Li, *J. Catal.*, 2025, **443**, 115996.

28 J. Xiang, P. Xu, J. Wang, Y. Shi, S. Yang, D. Tang, S. Tang and Y. Li, *J. Alloys Compd.*, 2024, **1002**, 175476.

29 S. Cao, B. Shen, T. Tong, J. Fu and J. Yu, *Adv. Funct. Mater.*, 2018, **28**, 1800136.

30 H. Yu, E. Haviv and R. Neumann, *Angew. Chem.*, 2020, **132**, 6278–6282.

31 M. Dan, S. Yu, W. Lin, M. Abdellah, Z. Guo, Z. Q. Liu, T. Pullerits, K. Zheng and Y. Zhou, *Adv. Mater.*, 2025, **37**, 2415138.

32 E. Haviv, L. J. Shimon and R. Neumann, *Chem.–Eur. J.*, 2017, **23**, 92–95.